Molecular spin qudits for quantum simulation of light-matter interactions Supplementary Information

F. Tacchino,[1] A. Chiesa,[2,3] R. Sessoli,[4,5] I. Tavernelli,[1] and S. Carretta[2,3]

[1] *IBM Quantum, IBM Research – Zurich, 8803 Rüschlikon, Switzerland*
[2] *Università di Parma, Dipartimento di Scienze Matematiche, Fisiche e Informatiche, I-43124 Parma, Italy*
[3] *UdR Parma, INSTM, I-43124 Parma, Italy*
[4] *Dipartimento di Chimica U. Schiff, Università di Firenze, I-50019 Sesto Fiorentino, Firenze, Italy*
[5] *UdR Firenze, INSTM, I-50019 Sesto Fiorentino, Firenze, Italy*

(Dated: June 18, 2021)

I. ENCODING OF THE RABI MODEL AND ELEMENTARY QUANTUM OPERATIONS

In this section, we provide some technical details about the encoding of atomic and photonic degrees of freedom on the proposed qudit-based architecture and on the implementation of the quantum operations required for VQE and digital quantum simulation algorithms.

We start form the target Rabi Hamiltonian presented in the main text (here and in the following, we assume $\hbar = 1$)

$$\mathcal{H} = \omega_a \sigma_z + \Omega a^\dagger a + 2G\sigma_x(a + a^\dagger) \tag{1}$$

where σ_i are spin-1/2 operators proportional to Pauli matrices, representing a two-level atom, and a is a bosonic annihilation operator. Assuming a hardware platform composed of a spin $s = 1/2$ coupled to a spin $S > 1/2$, we can immediately associate the atomic degrees of freedom to the first element via a direct mapping. In particular, if the hardware Hamiltonian is of the form

$$H_0 = g_{1z}\mu_B B S_{z1} + g_{2z}\mu_B B s_{z2} + D S_{z1}^2 + \sum_\alpha J_\alpha S_{1\alpha} s_{2\alpha} \tag{2}$$

we can identify $\sigma_i \leftrightarrow s_{i2}$. Unlike atomic systems, photonic degrees of freedom have in principle an infinite number of available discrete energy levels, namely Fock states $|n\rangle$, labeled by an integer number of excitations. However, as we will show in Sec. II, it is actually sufficient for our purposes to encode and manipulate a finite subset of Fock states, and precisely the lowest $n_{\mathrm{M}} + 1$ ones, where $n_{\mathrm{M}} \simeq$ 3-5 is the maximum number of photons allowed in the system. If we associate such truncated bosonic degrees of freedom with the spin S component of the hardware platform, we can thus accommodate $2S + 1$ levels, corresponding to $n_{\mathrm{M}} = 2S$ photons. For simplicity, we will assume that the eigenstates of H_0 are close to the uncoupled tensor products $|m_1\rangle|m_2\rangle$ of S_{z1} and s_{z2} eigenstates, with quantum numbers $m_1 = -S, -S-1, \ldots, S$ and $m_2 = \pm 1/2$ respectively. Such an approximation is actually well satisfied in the regime of small coupling that we adopt for our numerical calculations. However, while we may often refer to properties of the $|m_1\rangle|m_2\rangle$ states in the following, such as the fact that S_{x2} and S_{y2} operators contain matrix elements for $\Delta m_2 = \pm 1$ transitions, all numerical calculations are always performed with the true eigenstates of H_0.

Let us now consider the unitary transformation $\mathcal{U}(t) = e^{-i\mathcal{H}t}$ representing the time evolution operator for the Rabi Hamiltonian. As discussed in the main text, a useful approximation of $\mathcal{U}(t)$ can be obtained by the Trotter product formula

$$\mathcal{U}(t) \approx \mathcal{U}_N(t) = (e^{-i\omega_a s_{z2} t/N} e^{-i\Omega a^\dagger a t/N} e^{-i2G s_{x2}(a+a^\dagger)t/N})^N \tag{3}$$

As a first step, we observe that a rotation around the y axis of the spin $s = 1/2$, applied via the unitary operator $R_{y2}(\pi/2) = e^{-i\frac{\pi}{2}s_{y2}}$, transforms $\mathcal{U}_N(t)$ into

$$\tilde{\mathcal{U}}_N(t) = R_{y2}(\pi/2)\mathcal{U}_N(t)R_{y2}^\dagger(\pi/2) = (e^{-i\omega_a s_{x2} t/N} e^{-i\Omega a^\dagger a t/N} e^{-i2G s_{z2}(a+a^\dagger)t/N})^N \tag{4}$$

where we have used the fact that $R_{y2}(\pi/2)R_{y2}^\dagger(\pi/2) = \mathbb{I}$. Finally, in the spirit of the Holstein-Primakoff transformation [1], we can make the following associations between (truncated) bosonic and spin S operators:

$$\begin{aligned} \left(a^\dagger a\right)_{\text{truncated}} &= S_{z1} + S \\ \left(a + a^\dagger\right)_{\text{truncated}} &= \left(\frac{1}{\sqrt{S - S_{z1}}} S_{+,1} + S_{-,1}\frac{1}{\sqrt{S - S_{z1}}}\right) \equiv \Sigma_1 \end{aligned} \tag{5}$$

where $S_{\pm,1} = S_{x1} \pm iS_{y1}$. If $\delta = t/N$, we can now observe that each one of the N factors in the right hand side of Eq. (4) can be written, up to a global phase factor, as the product of three unitary operations

$$\tilde{\mathcal{U}}_N(t) = (e^{-i\omega_a s_{x2}\delta} e^{-i\Omega S_{z1}\delta} e^{-i2Gs_{z2}\Sigma_1\delta})^N = (R_{x2}(\omega_a\delta) R_{z1}(\Omega\delta) U_{z\Sigma}(2G\delta))^N \tag{6}$$

where $R_{z1}(\theta) = e^{-i\theta S_{z1}}$ (respectively, $R_{x2}(\theta) = e^{-i\theta s_{x2}}$) is a rotation of the spin $S > 1/2$ (respectively, $s = 1/2$) around the z axis (resp., x) and $U_{z\Sigma}(\theta) = e^{-i\theta s_{z2}\Sigma_1}$ is an entangling operation which describes the coupling between the atomic and photonic degrees of freedom. By inverting Eq. (4), we can now recast the digital quantum simulation protocol for the Rabi model on our qudit-based architecture in circuit form

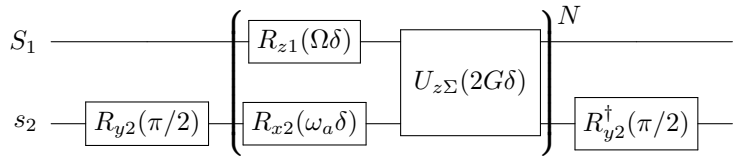

where the top line represents the $S_1 > 3/2$ qudit and the bottom line represents the $s_2 = 1/2$ component. We can now examine the actual hardware implementations of each of the required quantum logic operations represented above in terms of microwave control pulses.

In general terms, coherent control of the hardware is obtained via time-dependent magnetic field pulses along the x direction, inducing a Hamiltonian evolution of the form

$$H_p(t) = A_p(t)\cos(\omega_p t + \theta_p)(g_1\mu_B S_{x1} + g_2\mu_B s_{x2}) \tag{7}$$

where $A_p(t)$ is the time-dependent pulse field amplitude and we have explicitly taken into account the fact that, in principle, the magnetic field always couples to both the S_1 and s_2 spins. Such a Hamiltonian induces transitions between system eigenstates $|m_1\rangle|m_2\rangle$, whose dominant component is aligned with the z direction of the static field B, whenever the pulse frequency ω_p equals the corresponding energy difference

$$E^{m_1',m_2'}_{m_1,m_2} = E_{m_1',m_2'} - E_{m_1,m_2} \tag{8}$$

A set of well resolved transition frequencies, where all the physically allowed processes are associated to a different value of $E^{m_1',m_2'}_{m_1,m_2}$ (compared to the spectral width of the pulse), is therefore a key ingredient for achieving an effective control of the hardware operations.

a. Single qubit rotations $R_x(\theta)$ and $R_y(\theta)$ single qubit operations act by mixing the components of $|0\rangle$ and $|1\rangle$ elements of the computational basis, which are represented in our hardware setup by the (approximate) $|m_2\rangle = |\pm 1/2\rangle$ eigenstates of the spin 1/2. For example, the single $s_2 = 1/2$ spin rotations around the x and y axis appearing in the digital quantum simulation protocol outlined above can therefore be obtained by focusing on transitions of the form $E^{m_1,m_2\pm1}_{m_1,m_2}$. Notice that the operator $O_p = g_{1x}\mu_B S_{x1} + g_{2x}\mu_B s_{x2}$ appearing in the pulse Hamiltonian, see Eq. (7), contains the required matrix elements. The overall applied pulse must then be of the form

$$H^{x,y}_{p,2}(t) = \sum_{i=-S_1}^{S_1} A_i(t)\cos(E^{i,1/2}_{i,-1/2}t + \theta_p)(g_{1x}\mu_B S_{x1} + g_{2x}\mu_B s_{x2}) \tag{9}$$

The distinction between x and y rotations is obtained by selecting a phase offset $\theta_p = 0$ (for x) or $\theta_p = \pi/2$ (for y). At the same time, the rotation angle θ for a given transition is controlled by the pulse amplitude and duration (Δ_p) via the following relation

$$\theta = \int_{\Delta_p} dt A_p(t)\langle m_1, m_2|O_p|m_1, m_2\rangle \tag{10}$$

In order to achieve an effective operation which is independent of the state of the S_1 spin, the same rotation angle must be applied to all $(m_2, m_2 \pm 1)$ pairs, adjusting, e.g., the corresponding pulse duration or amplitude to account for differences in the corresponding matrix elements. We also notice that all the transitions appearing in Eq. (9) involve independent pairs of levels, and can thus be performed in parallel by linear superposition of the microwave pulses. In all numerical simulations reported in the main text, we adopt (unless stated otherwise) a gaussian pulse shape of the form

$$A_p(t) = A\exp\left(-\frac{(t-t_0)^2}{2\sigma^2}\right) \tag{11}$$

which provides good spectral selectivity.

b. Single qudit z rotations The $R_{z1}(\theta)$ operations on the spin $S > 1/2$ are achieved with semi-resonant pulses acting upon transitions of the form $E^{m_1+1,m_2}_{m_1,m_2}$. For every choice of m_1, a square pulse of the form

$$H_p^{\rm semi}(t) = A\cos(\omega_p t)O_p \tag{12}$$

with $A > 0$, $O_p = g_1\mu_B S_{x1} + g_2\mu_B s_{x2}$, frequency

$$\omega_p = |E^{m_1+1,m_2}_{m_1,m_2}| - {\rm sign}(E^{m_1+1,m_2}_{m_1,m_2})\delta, \tag{13}$$

and duration

$$\Delta_p = \frac{2\pi}{A|\langle m_1+1, m_2|O_p|m_1, m_2\rangle|}\frac{1}{\sqrt{1+\delta^2}}, \tag{14}$$

where

$$\delta = \frac{1-\phi}{\pi\sqrt{1-(1-\frac{\phi}{\pi})^2}}, \tag{15}$$

induces the transformation $|m_1, m_2\rangle \to e^{i\phi}|m_1, m_2\rangle$ and $|m_1+1, m_2\rangle \to e^{-i\phi}|m_1+1, m_2\rangle$ while leaving all other components of the hardware wavefunction untouched [2]. Assuming $S_1 = 3/2$ for simplicity, the desired operation

$$R_{z1}(\theta) = \begin{pmatrix} e^{-i\frac{3}{2}\theta} & 0 & 0 & 0 \\ 0 & e^{-i\frac{1}{2}\theta} & 0 & 0 \\ 0 & 0 & e^{i\frac{1}{2}\theta} & 0 \\ 0 & 0 & 0 & e^{i\frac{3}{2}\theta} \end{pmatrix} \tag{16}$$

can then be obtained as

$$\begin{pmatrix} e^{-i\frac{3}{2}\theta} & 0 & 0 & 0 \\ 0 & e^{-i\frac{1}{2}\theta} & 0 & 0 \\ 0 & 0 & e^{i\frac{1}{2}\theta} & 0 \\ 0 & 0 & 0 & e^{i\frac{3}{2}\theta} \end{pmatrix} = \begin{pmatrix} e^{-i\frac{3}{2}\theta} & 0 & 0 & 0 \\ 0 & e^{i\frac{3}{2}\theta} & 0 & 0 \\ 0 & 0 & e^{-i\frac{3}{2}\theta} & 0 \\ 0 & 0 & 0 & e^{i\frac{3}{2}\theta} \end{pmatrix} \begin{pmatrix} 1 & 0 & 0 & 0 \\ 0 & e^{-i2\theta} & 0 & 0 \\ 0 & 0 & e^{i2\theta} & 0 \\ 0 & 0 & 0 & 1 \end{pmatrix} \tag{17}$$

The first term on the right hand side is achieved by semi-resonant pulses targeting $m_1 = \pm 3/2 \leftrightarrow \pm 1/2$ transitions with $\phi = 3/2\theta$, while the second requires $m_1 = -1/2 \leftrightarrow +1/2$ and $\phi = 2\theta$. Notice that no approximation or digitalization error is made in using the product formula, due to the fact that all the operations are diagonal and thus commute. The above example is easily generalized to the case $S_1 > 3/2$.

c. Qubit-qudit entangling operations The entangling gate $U_{z\Sigma}(\theta) = e^{-i\theta s_{z2}\Sigma_1}$ can be seen as a conditioned set of transitions between $S_1 > 1/2$ qudit levels, controlled by the state of the $s_2 = 1/2$ qubit element. Indeed, the matrix Σ_1 has the form (we choose again $S_1 = 3/2$ for simplicity)

$$\Sigma_1 = \begin{pmatrix} 0 & \sqrt{3} & 0 & 0 \\ \sqrt{3} & 0 & \sqrt{2} & 0 \\ 0 & \sqrt{2} & 0 & 1 \\ 0 & 0 & 1 & 0 \end{pmatrix} \tag{18}$$

Let us define two auxiliary matrices

$$\Sigma_1' = \begin{pmatrix} 0 & \sqrt{3} & 0 & 0 \\ \sqrt{3} & 0 & 0 & 0 \\ 0 & 0 & 0 & 1 \\ 0 & 0 & 1 & 0 \end{pmatrix} \tag{19}$$

and

$$\Sigma_1'' = \begin{pmatrix} 0 & 0 & 0 & 0 \\ 0 & 0 & \sqrt{2} & 0 \\ 0 & \sqrt{2} & 0 & 0 \\ 0 & 0 & 0 & 0 \end{pmatrix} \tag{20}$$

Then, a unitary operation of the form $e^{-i\theta s_{z2}\Sigma_1'}$ corresponds to a rotation between the levels $|3/2,\pm1/2\rangle \leftrightarrow |1/2,\pm1/2\rangle$ (respectively, $|-1/2,\pm1/2\rangle \leftrightarrow |-3/2,\pm1/2\rangle$) of an angle $\pm\theta\sqrt{3}$ (respectively $\pm\theta$). The change in sign of the angle θ depends on the sign of m_2 and is, in fact, the source of the entangling correlations between the qubit and qudit hardware components introduced by this type of quantum gate. These transformations can be induced with pulses of the form

$$H_p^{z\Sigma}(t) = \sum_{j=\pm1/2}\sum_i A_{ij}(t)\cos(E_{i,j}^{i+1,j}t)(g_{1x}\mu_B S_{x1} + g_{2x}\mu_B s_{x2}) \tag{21}$$

where $i \in (-3/2, 1/2)$. The sign of θ can be changed by changing the sign of $A_{ij}(t)$, and the pulse duration is varied for different choices of i to account for the square root factors. Notice that such $\sqrt{n}$ terms are correctly associated to the states of the spin S_2 which encode n-photon states. Similarly to previous cases, all the pulses involved in Eq. (21) act on independent pairs of levels and can be performed simultaneously by operating with the linear superposition of all the required control signals. The operation $e^{-i\theta s_{z2}\Sigma_1''}$, induced by Σ_1'', can be described in similar terms, and promotes $\pm\theta\sqrt{2}$ rotations between the levels $|-1/2,\pm1/2\rangle \leftrightarrow |1/2,\pm1/2\rangle$. However, these transitions must be induced separately from the previous ones, in a sequential way, as they overlap on some eigenstates. Therefore, the overall transformation that can be achieved with this strategy is, e.g., the product

$$U_{z\Sigma''}(\theta)U_{z\Sigma'}(\theta) = e^{-i\theta s_{z2}\Sigma_1''}e^{-i\theta s_{z2}\Sigma_1'} \neq U_{z\Sigma}(\theta) \tag{22}$$

which is in general different from the desired $U_{z\Sigma}(\theta)$ due to the fact that $[\Sigma_1', \Sigma_1''] \neq 0$. However, the use of the approximation $U_{z\Sigma}(\theta) \simeq U_{z\Sigma''}(\theta)U_{z\Sigma'}(\theta)$ within the Trotter product formula of Eq. (6) has the sole effect of introducing additional contributions to the digitalization error. Additionally, as we will show in Sec. II, the use of a higher order formula in which $U_{z\Sigma}(\theta)$ is approximated with a more refined discretization

$$U_{z\Sigma}(\theta) \simeq \left(U_{z\Sigma''}(\theta/N_2)U_{z\Sigma'}(\theta/N_2)\right)^{N_2} \tag{23}$$

leads to an almost complete mitigation of this effect in most practical examples. By using Eq. (23), the general structure of the quantum circuit for the digital quantum simulation of the Rabi model becomes

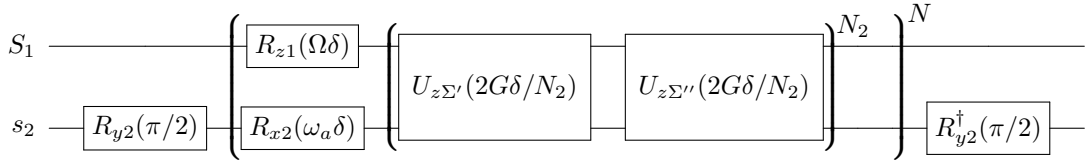

d. Variational quantum eigensolver The trial wavefunction used to approximate the ground state of the Rabi model with the VQE algorithm described in Fig. 1a of the main text can be constructed in practice by adapting some of the quantum gates introduced for digital quantum simulations. In particular, we assume an initial state with a de-excited atom and zero photons, i.e. $|\psi_0\rangle \simeq |m_1 = -S_1\rangle|m_2 = -s_2\rangle$ and we apply a sequence of parameterized unitary transformations based upon the single-qubit and qubit-qudit entangling operations described in previous paragraphs. In agreement with the applications reported in the main text, let us fix $S_1 = 3/2$, and split the matrix Σ_1' defined in Eq. (19) into two commuting parts

$$\Sigma_1' = \begin{pmatrix} 0 & \sqrt{3} & 0 & 0 \\ \sqrt{3} & 0 & 0 & 0 \\ 0 & 0 & 0 & 1 \\ 0 & 0 & 1 & 0 \end{pmatrix} = \begin{pmatrix} 0 & \sqrt{3} & 0 & 0 \\ \sqrt{3} & 0 & 0 & 0 \\ 0 & 0 & 0 & 0 \\ 0 & 0 & 0 & 0 \end{pmatrix} + \begin{pmatrix} 0 & 0 & 0 & 0 \\ 0 & 0 & 0 & 0 \\ 0 & 0 & 0 & 1 \\ 0 & 0 & 1 & 0 \end{pmatrix} = \bar{\varsigma}_1 + \varsigma_1 \tag{24}$$

The trial wavefunction is then obtained through the following sequence of gates

$$|\psi_{VQE}(\vec{\theta})\rangle = R_{y2}^{\dagger}(\pi/2)R_{x2}(\theta_4)e^{-i\theta_3 s_{z2}\Sigma_1''}e^{-i\theta_2 s_{z2}\bar{\varsigma}_1}e^{-i\theta_1 s_{z2}\varsigma_1}R_{y2}(\pi/2)|\psi_0\rangle \tag{25}$$

Here, $\vec{\theta}$ is a 4-dimensional vector of free parameters which are varied with the help of a classical optimization routine with the aim of minimizing the average expectation value of the Rabi Hamiltonian (mapped on the hardware degrees of freedom)

$$E_{\rm opt} = \min_{\vec{\theta}} E(\vec{\theta}) = \min_{\vec{\theta}} \left[\langle\psi_{VQE}(\vec{\theta})| \left[\omega_a s_{z2} + \Omega(S_{z1} + S_1) + 2G s_{x2}\Sigma_1\right] |\psi_{VQE}(\vec{\theta})\rangle\right] \tag{26}$$

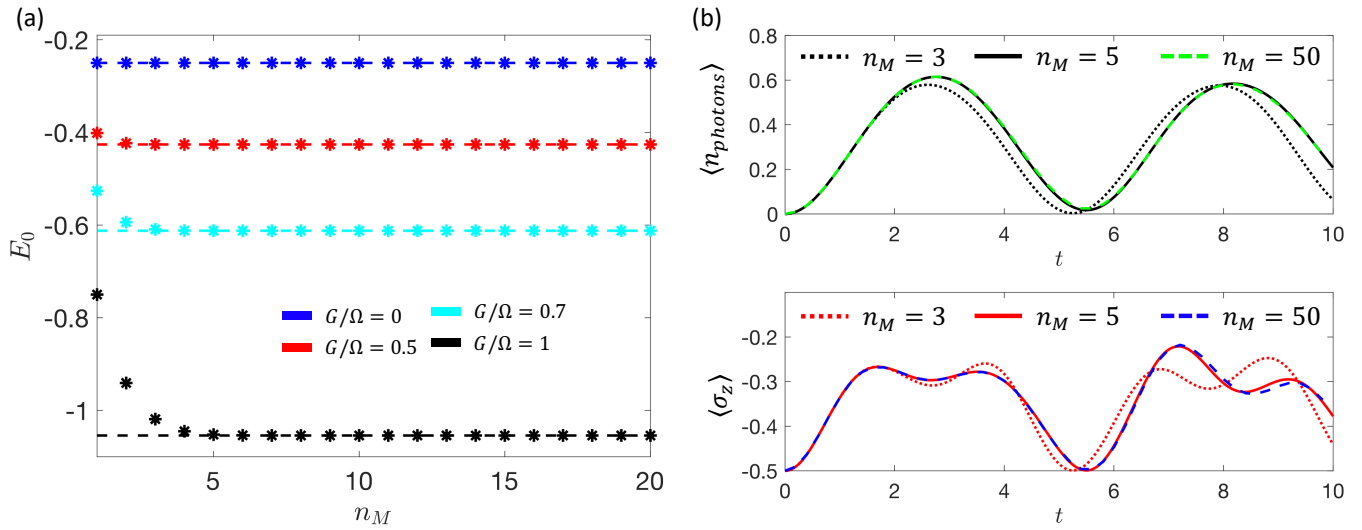

FIG. 1: Convergence of the exact numerical solution of the Rabi Hamiltonian with respect to the maximum number of photons n_M allowed in the system. (a) Ground state energy for increasing values of G/Ω. Dashed lines are reference values at convergence, computed with $n_M = 50$. (b) Time evolution of the average number of photons and atomic excitations for $G/\Omega = 0.5$. The dotted lines are computed with $n_M = 3$, solid lines with $n_M = 5$ and the dashed ones represent reference values with $n_M = 50$. Time evolution is computed through direct matrix exponentiation without the use of the Trotter product formula. In all panels, $\omega_a = 0.5\Omega$.

The operations appearing in Eq. (25) can be implemented in practice by using the pulse sequences described in Eq. (9) and Eq. (21). We explicitly notice that, due to its close relationship with time evolution operators, the combined effect of the unitary transformations in Eq. (25) preserves some important symmetries of the target Hamiltonian, such as the total parity of the number of excitations. It is also worth mentioning that, although not required in the examples presented in the main text, the complexity of the trial wavefunction $|\psi_{VQE}(\vec{\theta})\rangle$ can be increased by repeating the same structure more than once and introducing additional free parameters:

$$|\psi_{VQE}(\vec{\theta}_d)\rangle = \prod_{j=1}^{d} \left[R^{\dagger}_{y2}(\pi/2) R_{x2}(\theta_{j,4}) e^{-i\theta_{j,3} s_{z2} \Sigma''_1} e^{-i\theta_{j,2} s_{z2} \bar{\varsigma}_1} e^{-i\theta_{j,1} s_{z2} \varsigma_1} R_{y2}(\pi/2) \right] |\psi_0\rangle \tag{27}$$

This approach typically allows for better expressivity of the parametrized wavefunction, namely for a better coverage of the relevant portions of the target Hilbert space and therefore for better performances in the approximation of general quantum states. However, the introduction of many free parameters can also result in a more demanding classical optimization problem.

II. CONVERGENCE PROPERTIES

In this section, we provide some numerical results describing the convergence of the ideal solutions to both the ground-state approximation and the simulation of time evolution in terms of some tunable parameters such as photon number cutoff n_M and Trotter digitalization steps.

A. Maximum number of photons

In Fig. 1 we report some results describing the convergence of the spectral and time evolution properties of the truncated Rabi Hamiltonian

$$\mathcal{H}_{\text{truncated}} = \omega_a s_{z2} + \Omega(S_{z1} + S) + 2G s_{x2} \Sigma_1 \tag{28}$$

as a function of the maximum number of photons allowed in the system, $n_M = 2S_1$. All data are obtained via exact numerical diagonalization or exponentiation of the relevant matrices. The plots indicate that $n_M \simeq$ 3-5 is already sufficient to achieve good approximations in the regimes of interest.

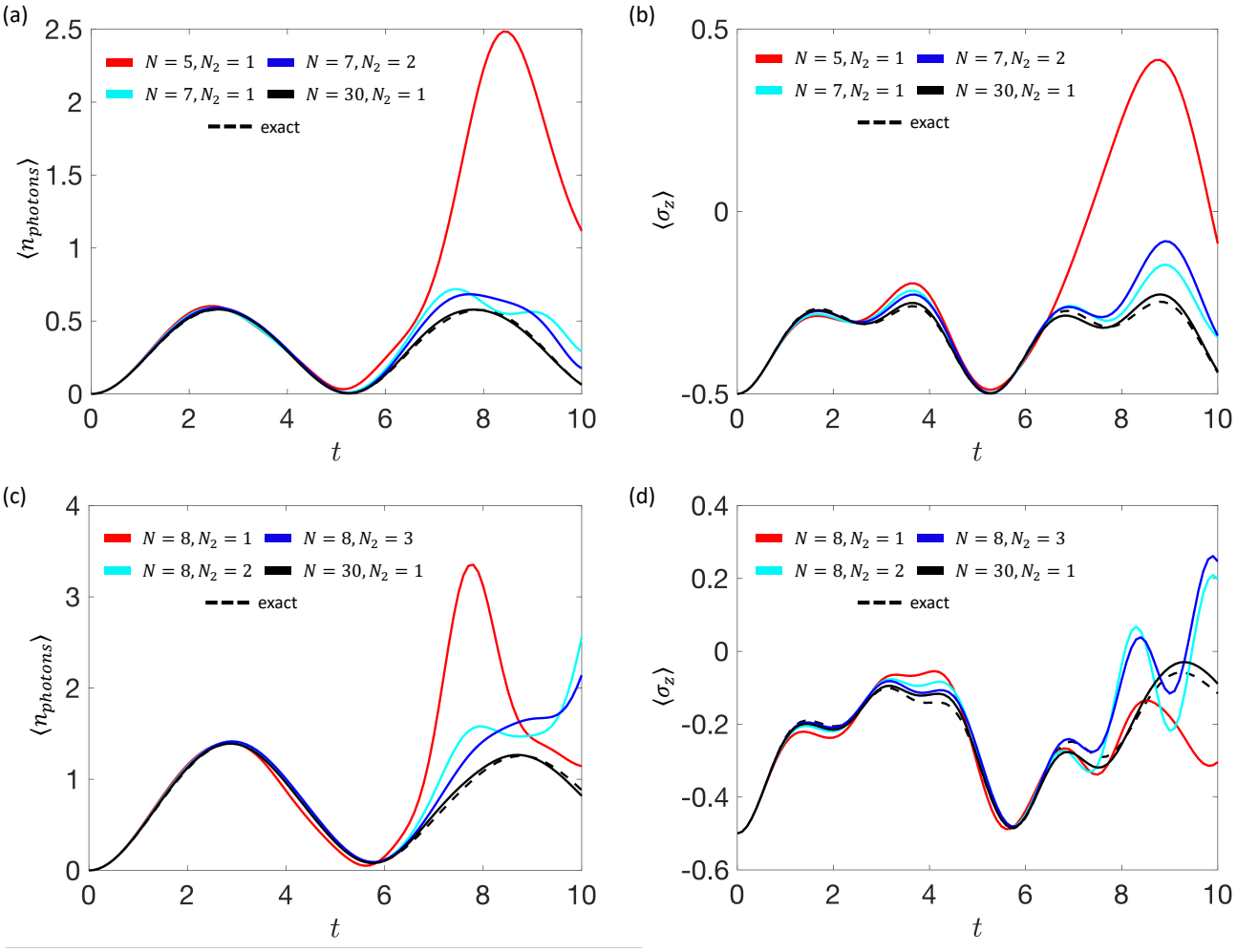

FIG. 2: Effect of digital approximation via Trotter product formula on the simulation of time evolution for the Rabi Hamiltonian. (a)-(b) $G/\Omega = 0.5$ with $S_1 = 3/2$ (c)-(d) $G/\Omega = 0.7$ with $S_1 = 5/2$. In all panels, $\omega_a = 0.5\Omega$ and the exact (dashed) curves with no digital error are obtained by matrix exponentiation of the total Rabi Hamiltonian truncated at $n_M = 2S_1$ photons.

B. Trotter product formula

The data reported in Fig. 2 describe the application of the general Trotter digitalization formula

$$\mathcal{U}(t) \approx \mathcal{U}_N(t) = R_{y2}^{\dagger}(\pi/2) \left[R_{x2}\left(\omega_a \frac{t}{N}\right) R_{z1}\left(\Omega \frac{t}{N}\right) \left[U_{z\Sigma''}\left(2G\frac{t}{NN_2}\right) U_{z\Sigma'}\left(2G\frac{t}{NN_2}\right)\right]^{N_2}\right]^{N} R_{y2}(\pi/2) \qquad (29)$$

introduced in the previous section for the digital quantum simulation of the Rabi model encoded on the proposed qudit-based architecture. All the plots are obtained numerically from Eq. (29) via matrix multiplication. Notice that for increasing G/Ω and S_1, more Trotter steps are needed to control the digitalization error. We also show the effect of the higher order approximation for $U_{z\Sigma}(\theta)$, see Eq. (23), which can improve the quality of the approximation (particularly at short simulated times) whenever $N_2 > 2$ at the cost of additional gate operations and, hence, longer sequences of hardware microwave pulses. For all plots reported in the main text, we set $N_2 = 2$ independently of N.

C. Size and depth of the VQE trial wavefunction

We conclude this section by describing the effect of system size (i.e. $n_M = 2S_1$) and of the depth of the variational quantum circuit on the VQE approximation to the ground state of the Rabi model. We refer to *depth* as the number

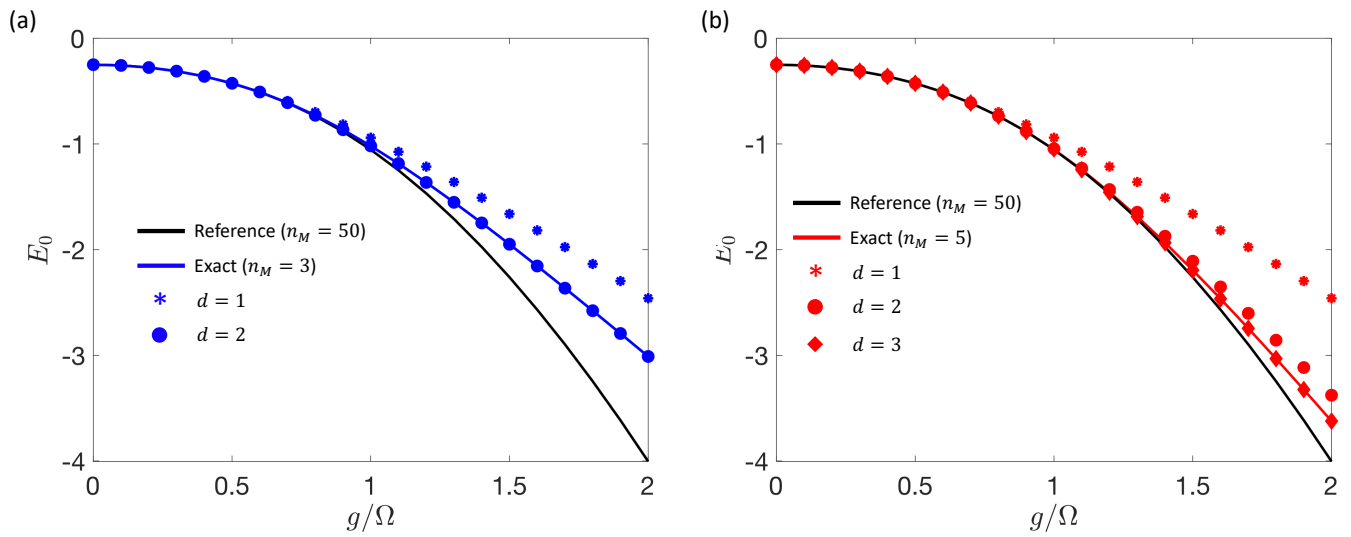

FIG. 3: Convergence of the VQE algorithm with for increasing $n_M = 2S_1$ and depth d of the trial wavefunction. (a) $S_1 = 3/2$ (b) $S_1 = 5/2$. In all panels, $\omega_a = 0.5\Omega$ and the number of variational parameters is equal to $(2S_1 + 1)d$. The data points for different values of d are computed numerically by constructing $|\psi_{VQE}(\vec{\theta}_d)\rangle$ via matrix multiplication according to Eq. (27) and using a classical Nelder-Mead optimization routine. Such results represent the outcome of an ideal VQE in the absence of hardware noise and quantum gate imperfections. Exact and reference solid curves are computed by direct diagonalization of the Rabi Hamiltonian truncated at $n_M = 2S_1$ and $n_M = 50$ (i.e. at convergence in the number of photons), respectively.

d of repetitions of the basic building block

$$V(\vec{\theta}) = R^{\dagger}_{y2}(\pi/2)R_{x2}(\theta_4)e^{-i\theta_3 s_{z2}\Sigma''_1}e^{-i\theta_2 s_{z2}\bar{\varsigma}_1}e^{-i\theta_1 s_{z2}\varsigma_1}R_{y2}(\pi/2) \tag{30}$$

appearing in the general form of the VQE trial wavefunction, see Eq. (27). The data reported in in Fig. 3 show that with $d = 1$ and $S_1 = 3/2$ the quality of the approximation is already very good over a wide range of G/Ω values and up to at least $G/\Omega \simeq 1$. Given that a single block $V(\vec{\theta})$ can be implemented on hardware with a pulse sequence which is significantly shorter and less demanding compared to any time evolution unitary transformation, these results are in fact particularly promising towards proof-of-principle experimental demonstrations.

[1] T. Holstein and H. Primakoff, Phys. Rev. **58**, 1098 (1940).
[2] A. Chiesa, P. Santini, D. Gerace, J. Raftery, A. A. Houck, and S. Carretta, Sci. Rep. **5**, 16036 (2015).